Published in final edited form as:
Anal Chem. 2012 March 6; 84(5): 2569–2575. doi:10.1021/ac2022822.

Modeling Analyte Transport and Capture in Porous Bead Sensors

Jie Chou[†], **Alexis Lennart**[‡,**], **Jorge Wong**[‡], **Mehnaaz F. Ali**[‡], **Pierre N. Floriano**[†,§], **Nicolaos Christodoulides**[†,§], **James Camp**[‡], and **John T. McDevitt**[†,§,*]

[†]Department of Bioengineering, Rice University, Houston, TX, 77007

[‡]Department of Chemistry, University of Texas at Austin, Austin, TX, 78712

[§]Department of Chemistry, Rice University, Houston, TX, 77007

Abstract

Porous agarose microbeads, with high surface to volume ratios and high binding densities, are attracting attention as highly sensitive, affordable sensor elements for a variety of high performance bioassays. While such polymer microspheres have been extensively studied and reported on previously and are now moving into real-world clinical practice, very little work has been completed to date to model the convection, diffusion, and binding kinetics of soluble reagents captured within such fibrous networks. Here, we report the development of a three-dimensional computational model and provide the initial evidence for its agreement with experimental outcomes derived from the capture and detection of representative protein and genetic biomolecules in 290μm porous beads. We compare this model to antibody-mediated capture of C-reactive protein and bovine serum albumin, along with hybridization of oligonucleotide sequences to DNA probes. These results suggest that due to the porous interior of the agarose bead, internal analyte transport is both diffusion- and convection-based, and regardless of the nature of analyte, the bead interiors reveal an interesting trickle of convection-driven internal flow. Based on this model, the internal to external flow rate ratio is found to be in the range of 1:3100 to 1:170 for beads with agarose concentration ranging from 0.5% to 8% for the sensor ensembles here studied. Further, both model and experimental evidence suggest that binding kinetics strongly affect analyte distribution of captured reagents within the beads. These findings reveal that high association constants create a steep moving boundary in which unbound analytes are held back at the periphery of the bead sensor. Low association constants create a more shallow moving boundary in which unbound analytes diffuse further into the bead before binding. These models agree with experimental evidence and thus serve as a new tool set for the study of bio-agent transport processes within a new class of medical microdevices.

Keywords

Modeling; porous beads; transport; reaction; binding kinetics; immunoassays; lab on a chip; microfluidics

[*]To whom correspondences should be addressed: mcdevitt@rice.edu; John McDevitt, Ph.D., 6100 Main Street, Department of Bioengineering, MS-142, Houston, TX 77005.

[**]In memoriam of Alexis Lennart, who received her doctorate degree on June 8th, 2011.

INTRODUCTION

With the ability to provide reliable results over a short time frame for low analyte concentrations, miniaturized detection systems promise to serve clinical, humanitarian, drug testing, homeland defense, military and environmental applications especially when they have multianalyte and multiclass capabilities.[1-3] The development of new medical micro-devices that exhibit strong analytical performance characteristics, are broadly responsive to a wide range of analyte classes, and are cost-effective has been difficult due mainly to complications in the integration of the various components and lack of functional concepts for selective and efficient bio-agent capture. The programmable bio-nano-chip (p-BNC) developed recently serves as a flexible detection ensemble that exhibits analytical performance characteristics rivaling established, macroscopic approaches. Employing three-dimensional “nano-nets” composed of agarose strands supported within 290 μm “micro-sponges” and fluorescent signal output from nanoparticles (nano), the p-BNC immobilizes and quantifies medically relevant species (bio) from complex samples within an enclosed mini flow chamber (chip). The p-BNC system with integrated microfluidic elements serves as an efficient and selective protein capture medium that is suitable for use in the analysis of complex fluid samples.

High performance porous bead-based arrays have been receiving a significant amount of attention for their potential use in point of care (i.e. near patient) applications.[4] Such porous bead-based systems have been used for the recognition and quantification of analytes ranging from ordinary ions such as calcium, to pH measurements, to complex immunological assays for the detection and quantitation of proteins, to oligonucleotide detection.[5-9] These studies have shown that porous bead sensors are associated with high performance characteristics, including the capacity to deliver high selectivity and detection of ultra-low bioanalyte concentrations using fully automated microassay platforms. Versus gold standard systems, such as enzyme-linked immunosorbent assay (ELISA), the p-BNC exhibits assay times measured in minutes rather than hours, limits of detection (LOD) two or more orders lower, and a multiplexed capacity of 10 or more concurrent analytes with appropriate internal controls. The strong analytical performance yielded by these medical micro-devices is attributed to the construction of the p-BNC in a way that harmonizes the attributes of elements on the nanometer, micrometer, and millimeter size regimes. Like ELISA, the bead-based p-BNC utilizes an immunoassay format; however, this feature presents as a matrix throughout the 3D bead, rather than as a 2D flat surface as in standard ELISA. The difference in orientation of the experimental building blocks within the BNC versus ELISA (capture antibody, detecting antibody, and antigen) likely contributes to the optimized assay performance.

Other studies have revealed enhanced performance from porous sensor ensembles as opposed to flat sensing surfaces.[10] For example, in studies by Zubtsov,[11] diffusion fluxes in hemispherical gel pads were found to be more efficient than in flat counterparts, and higher fluorescence signals were obtained from the gel pads versus microchips consisting of surfaces coated with antibodies, leading to higher sensitivity. The fluorescence signals for the hydrogel-based protein microchips demonstrated higher immobilization capacity than for

the microchips with surface-immobilized probes at the comparable kinetics of fluorescence saturation. Yang, et al. have studied porous agarose bead systems and shown that high uptake of analytes occurs as pore size increases.[12] Recent work using antibody-functionalized beads immobilized in porous hydrogels have exploited the internal mass transport properties of porous medium. Here, high antibody capacity and surface to volume ratios of porous support substrates were shown to achieve rapid assay times using small sample and reagent volumes.[13] Further, microfluidic systems utilizing porous gel pads as sensing elements have taken advantage of high loading densities and diffusive transport within porous media.[14, 15] Due to the high binding densities, such systems have the ability to detect low concentrations of antigen. However, in these systems, fluid is delivered via lateral flow. This flow over delivery, with poor efficiency of capture between antigen and immobilized antibodies, leads to long saturation times of several hours.[11, 15] To overcome inefficiencies in diffusion due to laminar flow in many microfluidic systems, the p-BNC system utilizes a flow-around and flow-through design. This unique design increases convective transport and capture efficiency between analytes and immobilized antibodies in sensing microbeads.

While several prior studies have examined immunoassays from a modeling perspective, most of these efforts have been limited to analyte capture localized on the 2D surfaces in a microfluidic channel. These prior efforts have investigated analyte binding and diffusion for both 2-site immunometric and competitive immunoassays, paying particular attention to effects of analyte concentrations and flow rates, sample and reagent volume as well as time constraints.[16-20] Important recent work by Bau and coworkers provided computational models to study transport and binding in agarose beads trapped in hot embossed wells in a lateral, flow over microfluidic channel,[21] yet these interesting prior studies focus exclusively on binding on the 2D external surface of a non porous bead. Further, in our previous work, we developed a 2D bead model to predict internal antibody binding densities and analyte porosities.[10] This 2D model agreed well with experimental results, however, internal transport and binding within a 3-dimensional porous bead resting in a flow-through well remains uncharacterized at this juncture.

In this paper, a microfluidic 3D model for analyte transport and capture within porous beads resting in flow-through pyramidal pit wells is developed and evaluated for the first time. To verify the new model, the spatial and temporal analyte distribution is compared using confocal image slices acquired for porous agarose beads functionalized for the capture of CRP, bovine serum albumin (BSA), and DNA molecular beacons.

MATERIALS AND METHODS

Computational Modeling

Simulations were run using COMSOL 3.5a (Burlington, MA) using the Chemical Engineering module's Navier-Stokes and Convection and Diffusion application modes. The 3D drawing of a 290μm bead resting in an inverted pyramidal pit with a 100×100μm base opening, 500×500μm top opening, and a 54.7° taper angle was constructed and imported from Auto-CAD 2011. The bead was modeled as a porous medium using Brinkman's Equation with a pore size of 400nm and porosity of 0.96, as based on previous work.[10] The

inlet flow rate was set to 1600μL·min^{-1} with an existing flow over rate of 300μL·min^{-1} and flow through bottom drain pressure of 1atm. Based on literature values,[22, 23] the reaction dissociation rate was set to 10^{-5} s^{-1} and association rates were in the range of 10^4 to 10^5 L·mol^{-1}s^{-1}. Based on typical concentrations used previously, 3000ng/mL of analytes were delivered to 9mg·mL^{-1} of loaded capture sites. These values represent a binding density of 3.0×10^{-7} mol·cm^{-3} and an analyte concentration in the bulk solution of 5.9×10^{-11} mol·cm^{-3}. To reduce the convergence time, the model was first solved using stationary Navier-Stokes, followed by the transient convection-diffusion and reaction rate equations.

Device Fabrication

Batches of 4% agarose beads were conjugated with anti-CRP, anti-BSA, and DNA probes, based on previous methods.[6] A protein labeling kit from Invitrogen (Carlsbad, CA) was used to link AlexaFluor®488 to protein antigen. Beads were manually loaded using forceps onto a silicon 4×5 array of anisotropically etched inverted flow-through pyramidal wells. This chip was sandwiched between two acrylic inserts with micro-milled and vinyl fluidic channels. The triplet was then sealed within astainless steel housing and connected to a 4 system peristaltic pump from FIALab (Bellevue, WA).

Assay Procedure

A solution of bovine serum albumin (BSA)-containing phosphate buffered saline (PBSA) was initially delivered to the bead array at 2000μL/min for 2 minutes to block non-specific binding sites and to remove bubbles. A solution containing the fluorescently-tagged target analyte, such as CRP, oligonucleotides, or BSA was then delivered to the array in recirculation. After 30 minutes delivery, the beads were washed with PBS for 2 minutes. Images were captured using an Olympus BX2 microscope (Center Valley, PA) and Leica TCS SP2 AOBS confocal system (Leica Integrated Systems Division, Malvern, PA) and analyzed using custom written ImageJ (NIH; Bethesda, MD) macros.

RESULTS AND DISCUSSION

Flow Studies Within the Microbead Array

To model the transport properties within the microbead array, we constructed a 3D model of a 3×4 array of beads resting in individual pyramidal pit wells that are created with an anisotropic etch of a Si (100) wafer. These supported beads, with diameters of 290μm, rest in etch pits with a top opening of 500×500μm and bottom opening of 100×100μm, which replicates the commonly used array structure reported previously. [5-8, 10] A size of 290μm for the diameter of the beads, has been found previously to be ideal for the particular geometry and dimensions of the bead holders used in this study. Additionally, beads of that size can be handled manually and loaded onto the array with tweezers. In this system, fluid aimed for analysis is delivered to the flow cell via an inlet, enters and bathes the microbead array from top to bottom, and ultimately exits through a drain (outlet) (Figure 1).

Here, the Navier-Stokes equation was used to establish a model of the fluid flow in the system. For directional clarity, the *xy*-plane is the horizontal lateral plane with *x* as the direction of delivered flow to the array, and *z* is the vertical axis. As shown in Figure 1A, the

flow profile exhibits the classical parametric profile due to no-slip conditions at the walls, while near the microarray, fluid flows down the wells to an underlying drain layer. With this simple geometry at the column of wells opposite the flow front, the fluid wraps back around towards the wells. In the geometry here employed the flow rate from well to well has a relative standard deviation of 14.8% with maximum flow concentrated at the front center side and minimum flow at the rear center side of the array.

To achieve a computational solution in a short time frame and eliminate non-uniformity of flow to each bead, we focused initially on a model of a single bead resting in a pyramidal pit well. Figure 1B shows velocity profiles of fluid, as it is delivered to subsequent adjacent beads, in and around each bead and ultimately down to drain. Volumetric flow increases as the cross sectional area of flow is reduced due to the increasing constriction to flow caused by the geometries of the pyramidal well and spherical bead. Because of the flow-through configuration, where fluid flows from the chamber above the beads through the array and down to drain, there exists a high pressure drop of 197.6 Pa at the bead well interface (Figure 1C). The existence of this pressure gradient across the bead serves as a key design element that may be used to control and optimize the analyte transport and capture issues as described below.

Molecular Level Insights to Analyte Capture

While delivered fluid serves to deliver the analyte species to the microbead array via convection, multiple factors simultaneously govern the transport process within the bead. Accordingly, it is crucial to elucidate and consider collectively both the chemical and physical processes inside the bead interior. First, transport is predominantly diffusion dominated because of the fibrous agarose network characterized with pore sizes around 500nm. Second, pressure driven flow, exterior to the bead, influences the amount of internal convection. This convection has the potential to drive analytes further into the bead. Finally, reaction kinetics between analytes and capture sites limits analyte penetration. Here, analytes, held back at the periphery of the bead, create an initial ring of signal that widens as sites become fully bound. The aggregation of signal in this moving boundary within the bead, not observed when modeling only the 2D surface of a bead, ultimately affects the final bead signal. Likewise, the incorporation of all three processes within the bead interior is necessary to build an accurate model that can serve as a tool to better understand analyte penetration and capture within such porous beads.

The Model

Computational fluid dynamics (CFD) requires several physical and chemical processes: fluidic flow, analyte transport via convection, diffusion and binding. Fluidic flow is governed by the incompressible Navier Stokes equation (1a) with the incompressibility constraint given by equation (1b). Flow through porous medium is defined by Brinkman's equation, a modified Navier-Stokes (3)[24]:

$$\rho\left(\frac{\partial u}{\partial t}+u\cdot\nabla u-f\right)-\nabla\cdot\sigma=0 \quad (1a)$$

$$\nabla \cdot u = 0 \quad (1b)$$

$$\rho\left(\frac{\partial u}{\partial t} + u \cdot \nabla u\right) + \nabla P - \eta\nabla^2 u = 0 \quad (2)$$

$$\nabla P = -\frac{\eta}{k}u + \frac{\eta}{\varepsilon_p}\nabla^2 u \quad (3)$$

Here, ρ is the fluid density (kg·m^{-3}); μ is the flow velocity (L·min^{-1}); f is the external force (kg·m·t^{-2}); P is the pressure (Pa); η is the dynamic viscosity (kg·m^{-1}s^{-1}); k is the permeability (m^2); and ε_p is the porosity (dimensionless). The Navier Stokes equation of incompressible flows in a 3D structure contains 3 momentum terms (eqn. 1a) for the flow, u, and one incompressibility constraint (eqn. 1b). The stress term, σ, can be expanded into pressure and viscosity components, resulting in equation 2. A detailed derivation is available as supplemental material.

The time-dependent concentration of species in the bead-well system are governed by the convection-diffusion equation:

$$\frac{\partial C}{\partial t} + u \cdot \nabla C = D\nabla^2 \mathrm{C} \quad (4)$$

Here, C (mol·L^{-1}) is the concentration of species, such as analyte in the bulk solution or immobilized antibodies, and D is the diffusion coefficient of the species (m^2·s).

Analyte binding to immobilized capturing sites is governed by the reaction rate law:

$$cAb + cAg \overset{k_{on},k_{off}}{\Longleftrightarrow} cAbAg \quad (5)$$

Here, *cAb* (mol·L^{-1}) is concentration of the immobilized binding sites; *cAg* (mol·L^{-1}) is the unbound analyte concentration; *cAbAg* (mol·L^{-1}) is the bound coupled pair; k_{on} (L·mol^{-1}·s^{-1}) is the association rate of binding between the analyte and unbound site; and k_{off} (s^{-1}) is the dissociation rate of release for the bound pair.

To solve these equations over a mesh of a simplified one-well subsystem, the flow, u, is calculated from time independent versions of equations (1-3). Boundary conditions for the inlet is specified as an initial velocity, outlet to drain is specified as atmospheric pressure, outlet to the 3 subsequent wells of the 3×4 array is specified as 75% of the inlet velocity, and side walls are specified as no-slip where u=0. Next, the concentration terms for *cAb*, *cAg*, and *cAbAg* are solved for from the solved values of u and the equations (4-5). The inlet is specified as the initial analyte concentration in bulk solution and outlets are specified as convective flux. For initial conditions on the bead, *cAb* is set to the initial concentration of

antibodies loaded on the bead, and *cAg* and *cAbAg* are set to zero. Concentrations of all three species are initially zero in the bulk solution. Only the diffusion coefficient of the species *cAg* is set to a non-zero value.

Coupling of Processes

En route to obtaining a comprehensive understanding of the transport properties associated with bioassays completed within bead-based porous media supported in the microsensor ensembles, we first explored the relative importance of diffusion, convection, and binding in their capacity to represent experimental observations.

In the diffusion only case, analytes quickly permeate the bead, as seen with complete saturation at 2.5min (Figure 2A). In this trivial case, representative of negative controls beads, permeated analytes do not bind and the bead develops no signal. In the binding only case (not shown), no binding occurs at the interior of the bead due to a lack of internal transport to deliver unbound analytes to available capture sites. However, in the binding and diffusion coupled case, unbound analytes initially bind and fill up open capture sites at the periphery of the bead. In Figure 2B, showing the bead *xy*-cross section at times 0.43min, 2.5min, and 43.4min, a dense ring of bound analytes initially develops at time 0.43min at the surface of the bead. However, as soon as these initial sites are bound, diffusion drives the transport of reagents further into the bead. As soon as the next layer of open sites is filled, the moving boundary of bound analytes leads to a widening ring around the bead as seen at time 43.4min.

Finally, because of the porous nature of the bead, internal convection drives analytes further into the bead, as shown in Figure 2C. While analytes are still held back as with the diffusion and binding case, convection allows analytes to transport further into the bead before binding. Under internal convection, signal penetration, as calculated by the full width, half aximum (FWHM) at time 43.4min, exhibited a 23.4% increase than the diffusion only case. Experimental confocal images of a CRP immune-capture (Figure 2D) were taken of the *xy*-medial plane under similar sample delivery conditions to verify the coupling of all three processes. Analytes are held back from completely saturating the bead as they initially bind to the outer surface of the bead. Further, confocal images were taken to examine the spatial distribution of bound analytes. Here, images taken under incremental *z*-slices of the bead (Figure 3A) after 30 minutes antigen delivery and subsequent wash agree well with the computational model (Figure 3B). The root mean square error between the FWHM of the CFD and confocal slices, normalized to the average width was 0.264. Due to the undulating motion of fluid delivery, the cross-like distribution of bound analyte, at the base of the bead in the model, is not observed experimentally. Further, the exact pore size inside the bead cannot be fully characterized. For 4% agarose beads reported here, we have found a range in pore size values to be between 80nm and 243nm based on microscopy measurements.[10]

Ellipsoidal Distribution

Due to the several orders of magnitude difference between the small internal pore sizes and the large bypass between the bead and walls of the well that hosts the bead, the bead acts as a constriction to flow in the macroscopic well environment. However, it was still unclear

whether internal convection affects the distribution of bound analyte. As such, analyte binding was examined under conditions with and without convection-driven internal flow. While the analyte penetration was higher under internal convection than without, as noted in the *xy*-cross sections (Figure 2B and 2C), direct comparison from the *xy*-plane did not provide sufficient validation. Accordingly, *xz*-cross sections were taken via confocal microscopy and also with our model. To examine the effects of internal convection, immunocapture of fluorescent CRP were completed as well as simulated with CFD under identical flow rate and incubation time conditions. Figure 4A, model under no internal convection, shows a uniform distribution of bound analytes where internal analyte transport is solely dependent on diffusion. Simulations under internal convection (Figure 4B), reveal the development of an asymmetrical ellipsoid. This ellipsoidal shape is a result of the contribution of variation of spatial bypass at each *xy*-plane to the capture efficiency. This shape, caused by both bead holder structure and pressure driven flow inside the bead, agrees well with experimental confocal images (Figure 4C). The undulating nature of fluid delivery from peristaltic pumps, causing the bead to shift during delivery, may explain slight discrepancies between experimental and computational results.

Pressure Driven Flow

The unique design of the porous bead supported in a flow-through microcontainer induces a microflow region around the bead that increases transport rates within the sensor ensemble.

The bead support exerts a localized pressure gradient across the bead, as seen in Figure 1C. Fluid, delivered to the array of beads, is forced to flow through each bead sensor. This localized flow creates a pressure gradient that is proportional to delivered flow rate. For flow rates from 6μL·min^{-1} to 1600μL·min^{-1}, the local pressure drop across the microcontainer increases proportionally from 4.04Pa to 1110Pa. These pressure drops correspond to local flow rates of 0.244 cm·s^{-1} to 51.0 cm·s^{-1}. The Reynolds number local to the bead-well interface plane was 4.66, equivalent to 4.28 times larger than that between the bead and ceiling.

The localized pressure gradient around the bead increases capture of analytes within the porous sensor, as follows. First, increase in convective transport drives analytes further into the bead. This internal fluid velocity was directly observed and measured using dyed yeast cells for superporous beads in a packed column by Gustavsson and co-workers.[25] Here, the internal flow velocity in 300-500μm superporous beads, with pore diameters of 30μm, was found to be 3% of the external flow velocity. Second, rate of analyte capture shifts from transport-limited to reaction-limited. At high flow rates, signal generated on the bead is limited by reaction kinetics rather than the replenishment of unbound analytes.

While higher flow rates enhance the transport and capture of analytes inside the bead, sample volume is typically low in diagnostic settings. The sample would run out before the allotted assay time. However, use of recirculation, as used previously,[10] can achieve higher capture in such low volume environments.

Internal Flow Rate

Due to difficulties in measuring internal fluid velocity experimentally for homogenous beads, this computational tool was used to examine internal flow rate under various pore sizes controlled by the concentration of agarose used to make the beads. Agarose concentrations of 0.5%, 4%, and 8% were used to create beads with pore sizes of 640nm, 243nm, and 140nm, respectively. Beads with higher agarose concentration or denser agarose network have smaller pore sizes. These pore sizes corresponding to respective agarose concentrations were determined based on previous microscopy measurements using SEM, TEM, and AFM.[10] Since lateral transport in porous substrates is often diffusion based, an understanding of the amount of convective dominated internal transport is important. The internal flow rate was calculated as the mean of the integrated flow velocities inside the bead. The average internal flow rate, measured for externally delivered flow rates of 6.25, 25, 100, 400, and 1600μL/min (Figure 4D), was linearly proportional ($R^2 = 1.00$) to the delivered inlet velocity. The internal flow rate increased as the pore size increased with an internal to external ratio of 1:3100, 1:1087, and 1:170 for pore sizes of 140nm, 243nm, and 640nm, respectively. This trend suggests that within the bead, as pore sizes decreases, diffusion dominates transport, but as pore size dramatically increases, convection will play a larger role.

Binding Kinetics on Distribution

These studies also reveal that the rate by which unbound analytes get captured on the beads depends on the binding kinetics. Due to the binding affinities of different analytes for their conjugate pairs, the association rate, k_{on}, varies between different analytes (Figure 5). As the analyte penetrates into the bead, the binding rate greatly affects the spatial analyte distribution. At high k_{on}, analytes have little time to diffuse into the bead before they quickly bind to open capturing sites. Due to the quick binding rates, unbound sites at the periphery of the bead fill up first, well before the interior sites do, as shown in the step-like cross sectional line profile for a high simulated k_{on} of 10^6 L·mol·s^{-1}.

Experimentally, this step-like distribution is seen for hybridization with DNA probes immobilized within the bead matrix with tagged complementary sequences (left inset). At low k_{on}, analytes have relatively longer unbound residence times within the porous network, allowing for longer diffusion times before being bound. This low binding rate leads to smooth, shallow sloped bound analyte distributions, as shown for a low k_{on} case of 10^4 L·mol·s^{-1}. The BSA binding, which occurs at a much slower rate than DNA hybridization, is shown as an example in the right inset. While lower k_{on} allows for higher penetration into the bead, the maximum signal at the bead periphery drops, as seen for a k_{on} of 10^4 L·mol·s^{-1} and BSA binding. For BSA, the higher penetration experimentally is likely due to a higher diffusion coefficient.[10] However, in order to isolate parameters, this value remained constant for this set of simulations. Further, directly correlated with the binding kinetics is the ratio of antigen to capturing antibody. In these studies, the *cAg/cAb* was 1.97×10^{-4}. Penetration will be higher for higher antigen concentrations as the capture of analytes would be limited by the rate of binding.

CONCLUSION

Porous agarose beads offer high surface to volume ratios and ability to be functionalized at high binding densities. When supported in microsensor ensembles with integrated flow elements, these hybrid sensor systems have the potential to provide both an index matched capture element as well as an efficient capture medium that supports rapid analyte binding. As such this study provides a foundation to understand internal analyte transport and binding within porous beads that are now moving into a variety of real-world clinical testing as diagnostic sensors. The ability to model, predict and optimize bioanalyte capture is a key step towards these novel medical microdevices moving into point of care settings where assay time and ability to sensitively measure biomarkers of interest are of critical importance[26].

The CFD model here presented, utilizes fundamental fluidic flow equations within porous and nonporous medium, convection and diffusion terms, and reaction rate equations between unbound analytes and capture sites, to accurately predict spatial and temporal distribution of analyte binding on beads sensors. Further, this model was verified experimentally by analysis of confocal images of beads used for the capture of a number of two protemic analytes, CRP, and BSA, as well as via DNA probe and target hybridization. From these studies it is found that the rate of binding kinetics affect the rate of signal development at the bead periphery as well as govern the depth of analyte penetration into the bead. Further, it is observed that the internal convection is linearly proportional to external delivered flow at a ratio range from 1:170 to 1:3100 for beads with pore sizes 140nm to 640nm.

Supplementary Material

Refer to Web version on PubMed Central for supplementary material.

Acknowledgments

Funding for this work was provided by the National Institute of Health through U01 Saliva Grant (NIH Grant No. 3 U01 DE017793-02S1 and 5 U01 DE017793-2).

References

1. Paitan Y, Biran I, Shechter N, Biran D, Rishpon J, Ron EZ. Monitoring aromatic hydrocarbons by whole cell electrochemical biosensors. Anal Biochem. 2004; 335(2):175–83. [PubMed: 15556555]
2. Porakishvili N, Fordham JL, Charrel M, Delves PJ, Lund T, Roitt IM. A low budget luminometer for sensitive chemiluminescent immunoassays. J Immunol Methods. 2000; 234(1-2):35–42. [PubMed: 10669767]
3. Szpunar J, Bettmer J, Robert M, Chassaigne H, Cammann K, Lobinski R, Donard OF. Validation of the determination of copper and zinc in blood plasma and urine by ICP MS with cross-flow and direct injection nebulization. Talanta. 1997; 44(8):1389–96. [PubMed: 18966875]
4. Derveaux S, Stubbe BG, Braeckmans K, Roelant C, Sato K, Demeester J, De Smedt SC. Synergism between particle-based multiplexing and microfluidics technologies may bring diagnostics closer to the patient. Anal Bioanal Chem. 2008; 391(7):2453–67. [PubMed: 18458889]
5. Ali MF, Kirby R, Goodey AP, Rodriguez MD, Ellington AD, Neikirk DP, McDevitt JT. DNA hybridization and discrimination of single-nucleotide mismatches using chip-based microbead arrays. Anal Chem. 2003; 75(18):4732–9. [PubMed: 14674448]

6. Christodoulides N, Dharshan P, Wong J, Floriano PN, Neikirk D, McDevitt JT. A microchip-based assay for interleukin-6. Methods Mol Biol. 2007; 385:131–44. [PubMed: 18365709]
7. Christodoulides N, Tran M, Floriano PN, Rodriguez M, Goodey A, Ali M, Neikirk D, McDevitt JT. A microchip-based multianalyte assay system for the assessment of cardiac risk. Anal Chem. 2002; 74(13):3030–6. [PubMed: 12141661]
8. Goodey A, Lavigne JJ, Savoy SM, Rodriguez MD, Curey T, Tsao A, Simmons G, Wright J, Yoo SJ, Sohn Y, Anslyn EV, Shear JB, Neikirk DP, McDevitt JT. Development of multianalyte sensor arrays composed of chemically derivatized polymeric microspheres localized in micromachined cavities. J Am Chem Soc. 2001; 123(11):2559–70. [PubMed: 11456925]
9. Ng JK, Selamat ES, Liu WT. A spatially addressable bead-based biosensor for simple and rapid DNA detection. Biosens Bioelectron. 2008; 23(6):803–10. [PubMed: 17949967]
10. Jokerst JV, Chou J, Camp JP, Wong J, Lennart A, Pollard AA, Floriano PN, Christodoulides N, Simmons GW, Zhou Y, Ali MF, McDevitt JT. Location of biomarkers and reagents within agarose beads of a programmable bio-nano-chip. Small. 2011; 7(5):613–24. [PubMed: 21290601]
11. Zubtsov DA, Savvateeva EN, Rubina AY, Pan'kov SV, Konovalova EV, Moiseeva OV, Chechetkin VR, Zasedatelev AS. Comparison of surface and hydrogel-based protein microchips. Anal Biochem. 2007; 368(2):205–13. [PubMed: 17544357]
12. Yang Y, Nam S-W, Lee NY, Kim YS, Park S. Superporous agarose beads as a solid support for microfluidic immunoassay. Ultramicroscopy. 2008; 108(10):1384–1389. [PubMed: 18550282]
13. Ikami M, Kawakami A, Kakuta M, Okamoto Y, Kaji N, Tokeshi M, Baba Y. Immuno-pillar chip: a new platform for rapid and easy-to-use immunoassay. Lab Chip. 2010; 10(24):3335–40. [PubMed: 20959907]
14. Chen L, Chen ZT, Wang J, Xiao SJ, Lu ZH, Gu ZZ, Kang L, Chen J, Wu PH, Tang YC, Liu JN. Gel-pad microarrays templated by patterned porous silicon for dual-mode detection of proteins. Lab Chip. 2009; 9(6):756–60. [PubMed: 19255656]
15. Arenkov P, Kukhtin A, Gemmell A, Voloshchuk S, Chupeeva V, Mirzabekov A. Protein microchips: use for immunoassay and enzymatic reactions. Anal Biochem. 2000; 278(2):123–31. [PubMed: 10660453]
16. Vijayendran RA, Ligler FS, Leckband DE. A Computational Reaction–Diffusion Model for the Analysis of Transport-Limited Kinetics. Anal Chem. 1999; 71(23):5405–5412. [PubMed: 21662737]
17. Zimmermann M, Delamarche E, Wolf M, Hunziker P. Modeling and optimization of high-sensitivity, low-volume microfluidic-based surface immunoassays. Biomed Microdevices. 2005; 7(2):99–110. [PubMed: 15940422]
18. Hu G, Gao Y, Li D. Modeling micropatterned antigen-antibody binding kinetics in a microfluidic chip. Biosens Bioelectron. 2007; 22(7):1403–9. [PubMed: 16879959]
19. Parsa H, Chin CD, Mongkolwisetwara P, Lee BW, Wang JJ, Sia SK. Effect of volume- and time-based constraints on capture of analytes in microfluidic heterogeneous immunoassays. Lab Chip. 2008; 8(12):2062–70. [PubMed: 19023469]
20. Fu E, Nelson KE, Ramsey SA, Foley JO, Helton K, Yager P. Modeling of a competitive microfluidic heterogeneous immunoassay: sensitivity of the assay response to varying system parameters. Anal Chem. 2009; 81(9):3407–13. [PubMed: 19361154]
21. Thompson JA, Bau HH. Microfluidic, bead-based assay: Theory and experiments. J Chromatogr B Analyt Technol Biomed Life Sci. 2010; 878(2):228–36.
22. Binding Kinetics Analysis with SPR: Interaction between Bovine Serum Albumin (BSA) and Anti-BSA. Biosensing Instrument Inc; 2010.
23. C-Reactive Protein. HyTest NEWS. 2008
24. Durlofsky, L.; Brady, JF. Analysis of the Brinkman equation as a model for flow in porous media. Vol. 30. AIP; 1987. p. 3329-3341.
25. Gustavsson P-E, Axelsson A, Larsson P-O. Direct measurements of convective fluid velocities in superporous agarose beads. Journal of Chromatography A. 1998; 795(2):199–210. [PubMed: 9528098]

26. Jokerst JV, Jacobson JW, Bhagwandin BD, Floriano PN, Christodoulides N, McDevitt JT. Programmable nano-bio-chip sensors: analytical meets clinical. Anal Chem. 2010; 82(5):1571–9. [PubMed: 20128622]

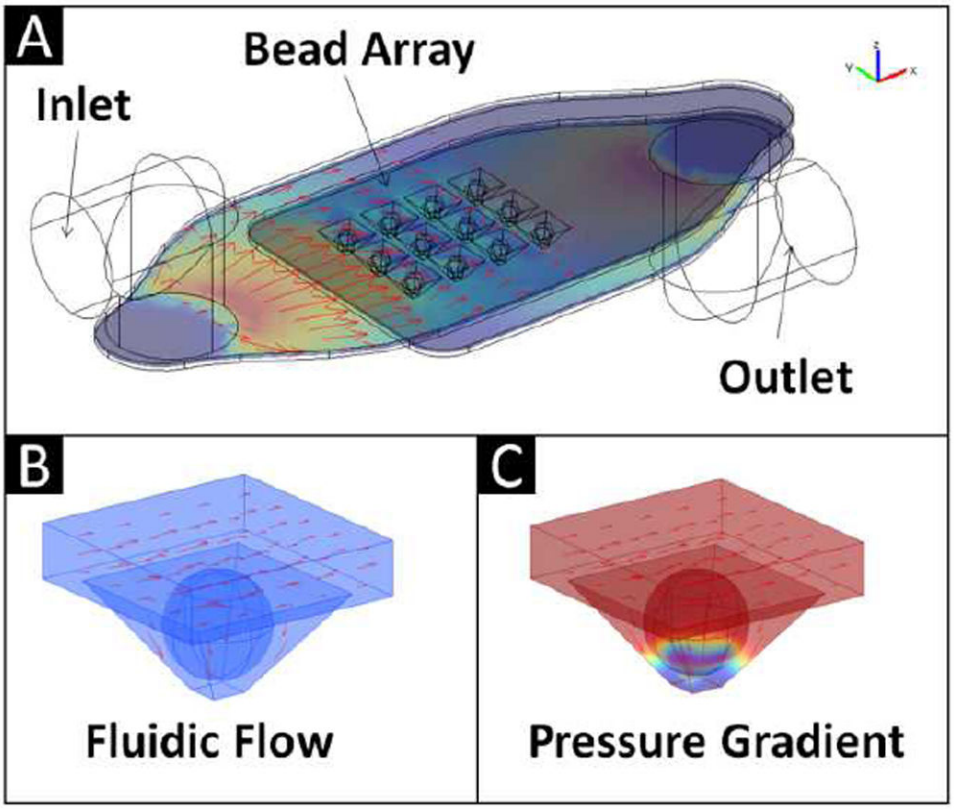

Figure 1.

A) Schematic showing fluid delivered via an inlet channel to an array of porous beads resting in individual anisotropically etched silicon wells. Red arrows show the flow trajectories of fluid to the array. B) A zoomed in view of a single bead showing that signal develops initially at the periphery of the bead. C) A pressure drop of 197.6 Pa, directly proportional to flow rate, exists at the bead well interface.

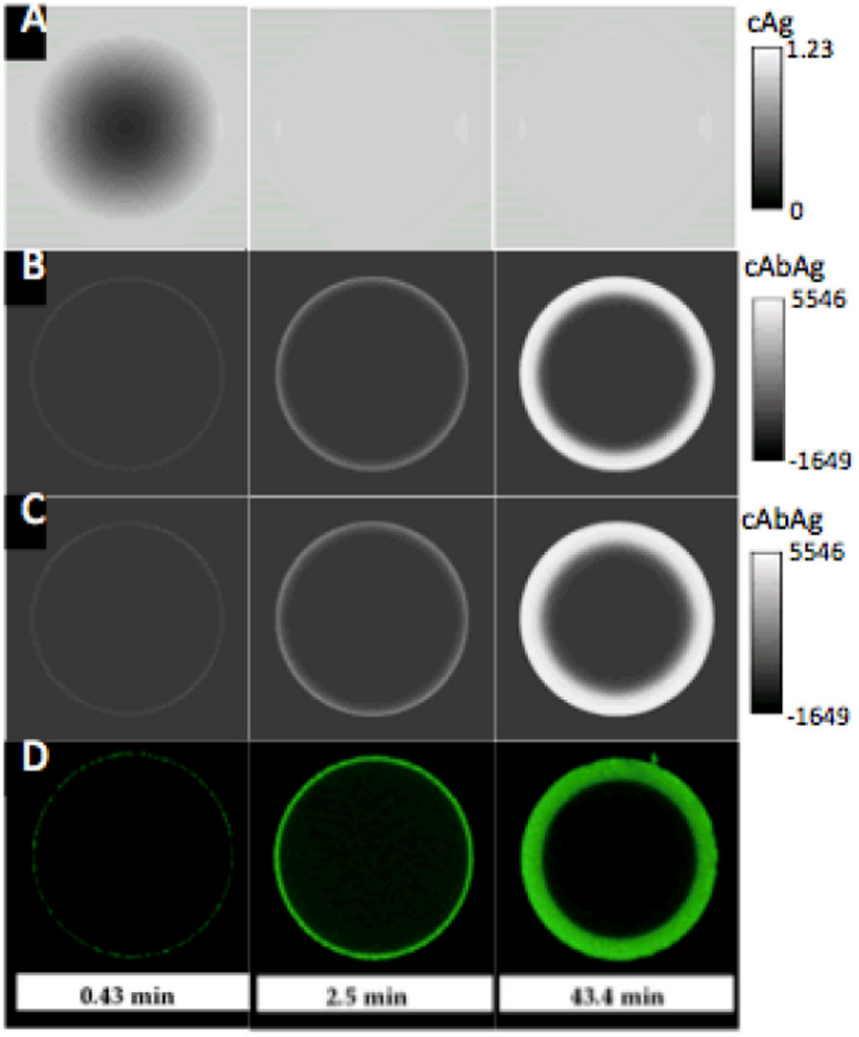

Figure 2.

Multiphysics modeling of a 243nm pore size bead showing xy-cross section at times 0.43min, 2.5min, and 43.4min shows the need for diffusion, convection, and binding. A) Under a diffusion only case, unbound CRP antigen (cAg) is able to completely saturate bead core. B) With the addition of binding reactions, analytes are held further back at bead periphery. Unbound analyte has less opportunity to be transported to the bead interior before it gets bound (cAbAg). C) When internal convection is turned out, the medial slice distribution is comparable with slightly higher penetration. D) Confocal images of bound CRP show agreement in temporal signal distribution.

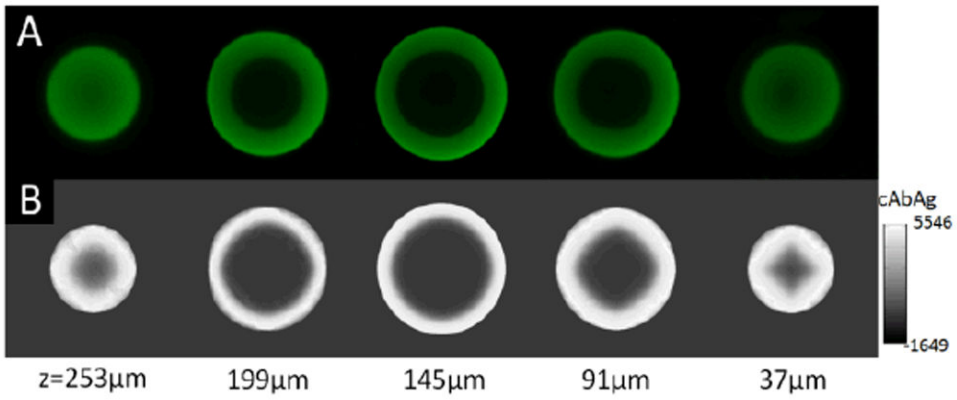

Figure 3.

Cross sectional xy-slices of CRP bead taken at different descending *z* planes with 54µm separation after 30 minutes analyte delivery shows agreement between confocal (A) and CFD (B). An internal core of unbound signal exists as analytes initially develop at bead periphery before penetrating radially towards the center of the bead.

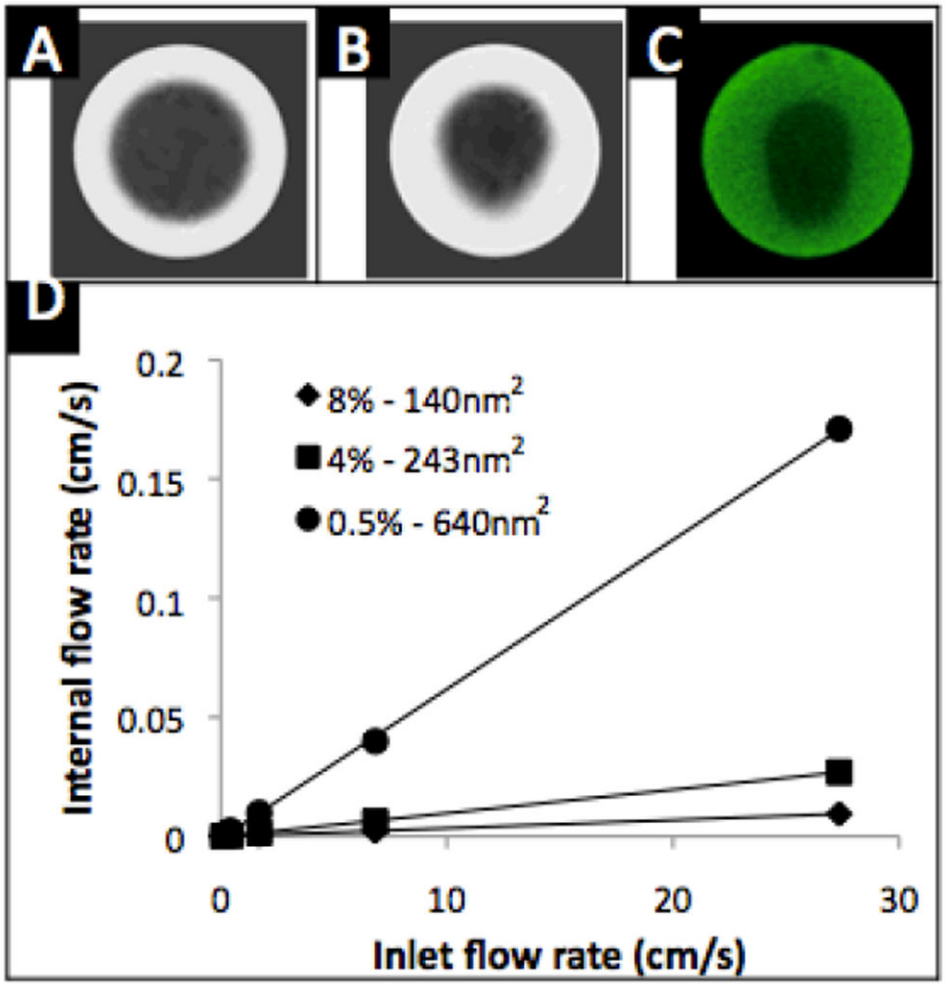

Figure 4.

A) XZ-cross sectional slices of CRP bead modeled under no internal convection. B) An ellipsoid develops due to internal convection and geometric positioning of bead in pyramidal well. C) Confocal slice in XZ-plane shows similar asymmetrical profile with modeling of binding distribution under internal convection condition. D) As reported by model, internal convection is linearly proportional to the delivered fluid. For 640nm, 243nm, and 140nm pore sizes, the internal to external ratio of 1:3100, 1:1087, and 1:170, respectively.

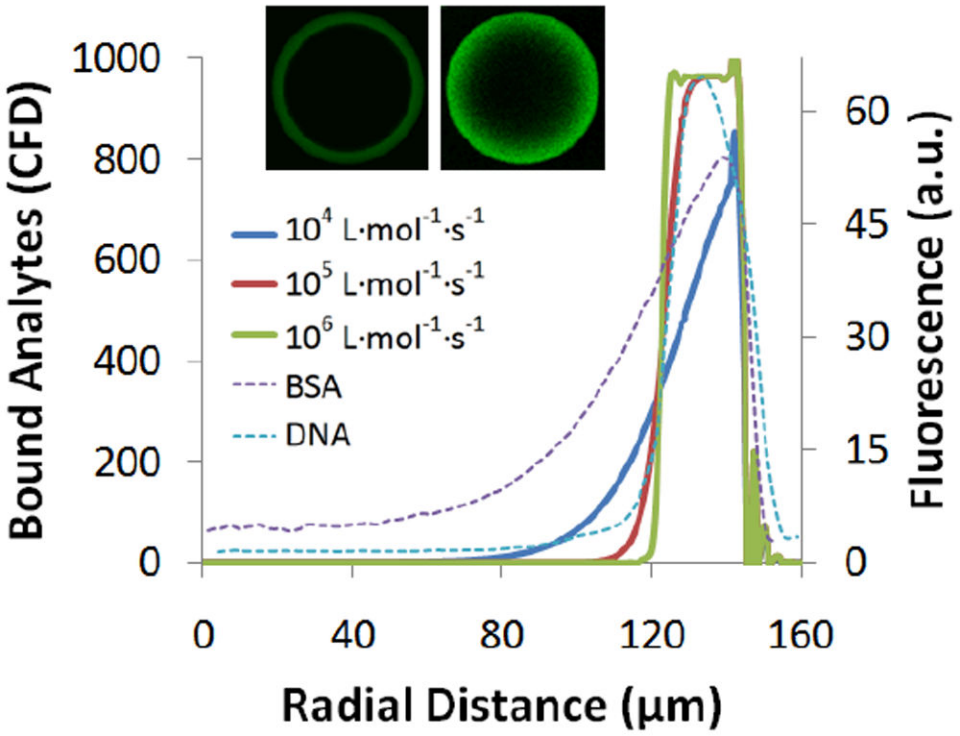

Figure 5.

Bound analyte distribution is affected by binding kinetic rates. At high association constants, k_{on}, of 10^6 L·mol^{-1}·s^{-1}, a steep moving boundary forms. Under a lower k_{on} (10^4 L·mol^{-1}·s^{-1}), bound analytes exhibit a gradual descent towards to bead center due to longer unbound transport duration into the bead before binding. Confocal examples showing high k_{on} for DNA hybridization using molecular beacons (inset, left) and low k_{on} for BSA (inset, right) exhibit steep and shallow moving boundary distributions.